

X-ray and radio data obtained by XMM-Newton and VLA constrain the stellar wind of the magnetic quasi-Wolf-Rayet star in HD45166

P. Leto¹, L.M. Oskinova², T. Shenar³, G.A. Wade⁴, S. Owocki⁵, C.S. Buemi¹, R. Ignace⁶, C. Trigilio¹, G. Umama¹,
A. ud-Doula⁷, H. Todt², W.-R. Hamann²

¹ Osservatorio Astrofisico di Catania, INAF, Via S. Sofia 78, I-95123 Catania, Italy
e-mail: paolo.letto@inaf.it

² Institute for Physics and Astronomy, University Potsdam, Karl-Liebknecht-Str. 24/25, D-14476 Potsdam, Germany
e-mail: lida@astro.physik.uni-potsdam.de

³ The School of Physics and Astronomy, Tel Aviv University, 6997801 Tel Aviv, Israel

⁴ Department of Physics and Space Science, Royal Military College of Canada, PO Box 17000, Kingston, ON K7K 7B4, Canada

⁵ Department of Physics and Astronomy, University of Delaware, 217 Sharp Lab, Newark, DE 19716, USA

⁶ Department of Physics & Astronomy, East Tennessee State University, 173 Sherrod Drive, Johnson City, TN 37614, USA

⁷ Penn State Scranton, Pennsylvania State University, 120 Ridge View Drive, Dunmore, PA 18512, USA

March 11, 2025

ABSTRACT

Context. Recently, a powerful magnetic field was discovered in the hot helium star classified as a quasi-Wolf-Rayet (qWR) star of $\sim 2 M_{\odot}$, member of the HD 45166 system. Upon its explosion as a core-collapse supernova, it is expected to produce a strongly magnetic neutron star – a magnetar. Among the key parameters governing the pre-supernova evolution is the amount of mass lost via stellar wind. However, the magnetic nature of this helium star is expected to affect its stellar wind making the estimation of the wind parameters uncertain.

Aims. We report the first observations of HD 45166 in X-rays with the XMM-Newton telescope and in radio with the VLA interferometer array. By placing the observation results in a theoretical framework, we aim to provide a reliable estimate of the wind strength of the magnetic qWR star.

Methods. The X-ray properties are explained in the framework of the magnetically-confined wind shock (MCWS) scenario, and the semi-analytic XADM model is applied to reproduce the X-ray emission. The thermal radio emission of the wind and its absorption effect on possible gyro-synchrotron emission from the underlying dipolar magnetosphere, sampled in 3D, are computed by integrating the radiative transfer equation.

Results. We did not detect radio emissions, this enabled us to set sensitive upper limits on the radio luminosity. The magnetic qWR star is a slow rotator, comparison with models reveals that the possible acceleration mechanisms occurring within its dynamical magnetosphere are not as efficient as in fast-rotating magnetic ApBp-type stars. In contrast, the system is detected in X-rays with $\log(L_X/L_{\text{bol}}) \sim -5.6$. Using suitable models, we constrain the mass lost from this magnetic quasi-Wolf-Rayet star as $\dot{M} \approx 3 \times 10^{-10} M_{\odot} \text{ yr}^{-1}$.

Conclusions. This novel empirical estimate of the mass-loss rate in a $\sim 2 M_{\odot}$ helium star confirms that it maintains super-Chandrasekhar mass till collapse and can produce a magnetar as its final evolutionary product.

Key words. X-rays: stars – Radio continuum: stars – stars: Wolf-Rayet – stars: winds, outflows – stars: mass-loss – stars: magnetars

1. Introduction

The binary system HD 45166 consists of a hot helium star and a B7 V-type star (Willis & Stickland 1983) bound with an orbital period of 22 yr (Shenar et al. 2023). The optical spectrum of the helium star is dominated by emission lines of carbon, nitrogen, and oxygen in high ionization states, hence warranting its Wolf-Rayet (WR) spectral classification (Anger 1933; Neubauer & Aller 1948; Hiltner & Schild 1966). The relatively low luminosity of the helium star compared to classical WR stars, in combination with its uniquely narrow emission lines and unusual abundance pattern, gave rise to its designation as a quasi-Wolf-Rayet (qWR) star (van Blerkom 1978). The mass of the qWR star was originally estimated at $0.5 M_{\odot}$ (Willis & Stickland 1983), then raised to $\approx 4 M_{\odot}$ (Groh et al. 2008), and finally revised as $M_* = 2.03 \pm 0.44 M_{\odot}$ (Shenar et al. 2023). While this mass is at the lower limit needed for core-collapse (Woosley

et al. 1995) the final fate of the qWR component is uncertain, and whether or not the star will produce a supernova (SN) will sensitively depend on the amount of mass it will lose until core-collapse.

The characteristics of the helium star in HD 45166 make it a prototype for super-Chandrasekhar mass stars stripped of their outer hydrogen layers. Helium stars of such masses are generally thought to form via interactions among components in close binaries (Podsiadlowski et al. 1992; Yungelson et al. 2024). This evolutionary channel can lead to the formation of helium-rich stars significantly less massive than the classical WR stars (i.e. $\lesssim 10 M_{\odot}$) (Hamann et al. 2019; Sander et al. 2019; Shenar et al. 2020). Binary evolution models predict that stripped stars are hot and numerous; as such, they could be among the dominant ionizing sources in star-forming galaxies and may represent the bulk of progenitors of stripped supernovae (Dionne & Robert 2006; Göteborg et al. 2018; Doughty & Finlator 2021). Finding

Table 1. Parameters of the magnetic qWR star in the HD 45166 system.

Parameter	Unit	Value	Reference
Distance: D	parsec	991^{+38}_{-33}	Bailer-Jones et al. (2021)
Bolometric luminosity: $\log(L/L_{\odot})$	-	3.83 ± 0.05	Shenar et al. (2023)
Reddening: E_{B-V}	magnitude	0.210 ± 0.010	Shenar et al. (2023)
Temperature: T_*	kK	56.0 ± 6.0	Shenar et al. (2023)
Mass: M_*	M_{\odot}	2.03 ± 0.44	Shenar et al. (2023)
Radius: R_*	R_{\odot}	0.88 ± 0.16	Shenar et al. (2023)
Rotation period: P_{rot}	day	124.8 ± 0.2	Shenar et al. (2023)
Average magnetic field: $\langle B \rangle$	kG	43.0 ± 2.5	Shenar et al. (2023)

super-Chandrasekhar-mass helium stars stripped by binary interactions turned out to be difficult (Ramachandran et al. 2023; Drout et al. 2023; Gilkis & Shenar 2023), and over a long time, the qWR star in the HD 45166 system was the only well-studied candidate.

Of special interest is the mass-loss rate of these objects, which determines the properties of the pre-collapse core. Radiation fields of hot, OB- and WR-type, stars drive stellar winds (Castor et al. 1975). Previous analyses of the optical spectrum of the qWR star by means of latitude-dependent wind models derived a mass-loss rate of $\dot{M} \approx 2 \times 10^{-7} M_{\odot} \text{ yr}^{-1}$ (with: equatorial wind velocity $V_{\infty}^{\text{eq}} \approx 425 \text{ km s}^{-1}$; polar terminal wind velocity $V_{\infty}^{\text{pole}} \approx 1200 \text{ km s}^{-1}$; Willis & Stickland 1983; Willis et al. 1989; Groh et al. 2008). These values are significantly different from the theoretical predictions. Vink (2017) explored the parameter space characterizing winds from helium stars. The mass of the helium star (or equivalently its luminosity given the mass-luminosity relation) has been varied in the range from $60 M_{\odot}$ to 0.6 solar masses, with a fine tuning in the range 2–20 M_{\odot} . Once assigned metallicity and mass, the Monte Carlo modeling approach performed by Vink (2017) provides both the mass-loss rate and the terminal wind velocity. In particular, the mass-loss rate predicted for a $2 M_{\odot}$ star at Solar metallicity is $\dot{M}_{\text{th}} \approx 4 \times 10^{-9} M_{\odot} \text{ yr}^{-1}$, while the predicted wind velocity is $V_{\infty}^{\text{th}} \approx 2650 \text{ km s}^{-1}$.

The striking difference between the empirically measured mass-loss rate and wind velocity of the qWR star and the theoretical predictions have been noticed already by Vink (2017). However, the recent discovery of strong magnetic field on the qWR star suggests that its wind is strongly affected by magnetic field and calls for new approaches in evaluating its stellar wind parameters. In this paper we address this problem using new X-ray and radio observations.

The qWR possesses an exceptionally strong magnetic field of $\langle B \rangle \sim 43 \text{ kG}$. This breaks the record held by Babcock’s Star ($\sim 34 \text{ kG}$; Babcock 1960) making the qWR the most strongly magnetic non-degenerate star known. The qWR is likely a merger product in an initially triple system, with the non-magnetic B7 V component being an original tertiary, and is predicted to end its life as a strongly magnetic neutron star: a magnetar (Shenar et al. 2023).

The high magnetic field of the qWR star plays a major role in regulating its mass-loss. The magnetic field affects the free radial flow of the stellar wind up to a certain distance, named Alfvén radius (R_A), leading to a so-called confined wind structure. Hence, the spectrum of the qWR star forms in its magnetosphere, which must be taken into account in empirical mass-loss rate measurements.

The magnetic star in the HD 45166 system is a very slow rotator, its rotation period exceeds 100 days (Table 1). This is

a suitable condition for originating a dynamical magnetosphere (DM) which commonly characterizes the slowly rotating massive magnetic stars with a radiatively driven stellar wind (Petit et al. 2013). Furthermore, the combined presence of wind and magnetic field allows to place the qWR in the context of other hot massive magnetic stars such as ApBp-type stars which are, in general, X-ray and radio sources (Drake et al. 1987, 1994; Linsky et al. 1992; Leone et al. 1994; Oskinova et al. 2011; Nazé et al. 2014). Production of X-rays in magnetic hot stars is usually explained by the cooling of a fraction of their stellar winds, heated to a few million degrees by strong shocks resulting from the collision of streams confined by a magnetic field (magnetically confined wind shock, MCWS, model) (Babel & Montmerle 1997; ud-Doula & Nazé 2016). This helps to explain why some magnetic stars are more X-ray luminous compared to their non-magnetic counterparts (Oskinova et al. 2011; Nazé et al. 2014).

Magnetohydrodynamic (MHD) simulations predict that the continuous supply of wind material to the magnetospheres in slowly-rotating stars is balanced by the plasma infall back onto the stellar surface (ud-Doula & Owocki 2002; ud-Doula et al. 2008, 2013). Beyond the Alfvén radius the breaking of the magnetic field lines should lead to particle acceleration (Usov & Melrose 1992). Fast non-thermal electrons power both incoherent non-thermal gyro-synchrotron and coherent auroral radio emission (Trigilio et al. 2000; Das et al. 2022) and, in some cases, also non-thermal X-rays of auroral origin (Leto et al. 2017; Robrade et al. 2018).

Thus, radio and X-ray observations are excellent probes of conditions in stellar magnetospheres. To gain insight into the wind properties of the qWR star and its magnetosphere we obtained new observations in X-ray and radio domains. In Sect. 2 we describe the observations and data reduction. In Sect. 3 we report the observational results directly derived from the analysis of the X-ray (Sect. 3.1) and radio (Sect. 3.2). In Sect. 4.1 we provide the theoretically expected X-ray spectrum; in Sect. 4.2 we describe how the stellar wind is affected by its strong magnetic field. The physical mechanism affecting the radio emission are explored in Sect. 5; in Sect. 5.1 we discuss the possible non-thermal electron production and, after taking into account the frequency dependent absorption effect due to the large-scale distributed wind plasma, the upper limit of the corresponding non-thermal radio emission has been calculated in Sect. 5.2, finally, in Sect. 5.3, we place our results in a general framework that includes the O-type magnetic stars. In Sect. 6 we present our conclusions and discuss how the forthcoming sensitive radio facilities may be useful for the science case discussed in this paper.

Table 2. Log of the VLA Observations of HD 45166. Array Config C. Code: 22B-314.

Date-OBS	UTC	T. on Sou. (minutes)	ν (GHz)	$\Delta\nu$ (GHz)	RMS (μ Jy/beam)	FWHM ("×")	PA (deg)
2022 Nov 9	13:13:47.5	19	5.5	2	≈ 8	4.88×3.69	50.57
2022 Nov 9	13:38:40.5	19	9	2	≈ 7	3.60×2.18	54.22
2022 Nov 16	13:24:40.5	26	15	6	≈ 5	2.26×1.37	54.88

2. Observations and data reduction

2.1. Radio

The radio observations were performed at the Very Large Array (VLA) National Radio Astronomy Observatory in November 2022, the observing log is reported in Table 2. The observations were conducted in three bands: the C-band, centered at $\nu = 5.5$ GHz; the X-band, centered at $\nu = 9$ GHz; and the Ku-band, centered at $\nu = 15$ GHz. For the C and X bands the adopted hardware setup allowed to observe a bandwidth of 2 GHz width (8-bit digital samplers), whereas the adopted setup for the Ku-band observations allowed recovering flux within a wider spectral range, bandpass of 6 GHz using the 3-bit digital samplers.

To calibrate the flux scale and the receiver’s response within the spectral range covered by the VLA receivers (bandpass calibration), the radio galaxy 3C286 (1331+305) was observed as primary calibrator in each observing band. To calibrate the amplitude and phase of the complex gain, the standard VLA calibrator J0613+1306 was cyclically observed for each band during the observing scans. J0613+1306 is a point-like radio source located close to the sky position of HD 45166 (about 6° away) with an almost flat radio emission level (≈ 0.5 Jy) in the range 5–15 GHz. The observations have been processed through the VLA Calibration Pipeline (version 2022.2.0.64), which is designed to handle Stokes I continuum data, operating within the Common Astronomy Software Applications (CASA) package (release 6.4.1). Images of the sky region centered at the target position have been obtained using the task `TCLEAN` (number of Taylor terms 2, number of clean iterations 40000).

HD 45166 is located in a sky region not contaminated by strong radio sources and the radio maps of the total intensity (Stokes I) show no issues. In fact, we measured low noise levels in each band (RMS $< 8 \mu$ Jy/beam, see Table 2), which nearly coincide with the nominal levels expected in each band, corresponding to the bandpass adopted and the available times on source, as given by the VLA exposure calculator¹, confirming the goodness of the VLA observations. Despite the high-quality radio measurements, HD 45166 is not detected.

2.2. X-rays

X-ray data were acquired with the X-Ray Multi-Mirror Mission (XMM-Newton) of the European Space Agency (ESA). XMM-Newton has three X-ray telescopes that illuminate five different instruments, which always operate simultaneously and independently. The useful data were obtained with the three focal instruments: MOS1, MOS2, and pn, which together form the European Photon Imaging Camera (EPIC). The EPIC instruments have a broad wavelength coverage of $1.2 - 60 \text{ \AA}$ and allow low-resolution spectroscopy with ($E/\Delta E \approx 20 - 50$). Throughout this paper, X-ray fluxes and luminosities are given for the full energy band.

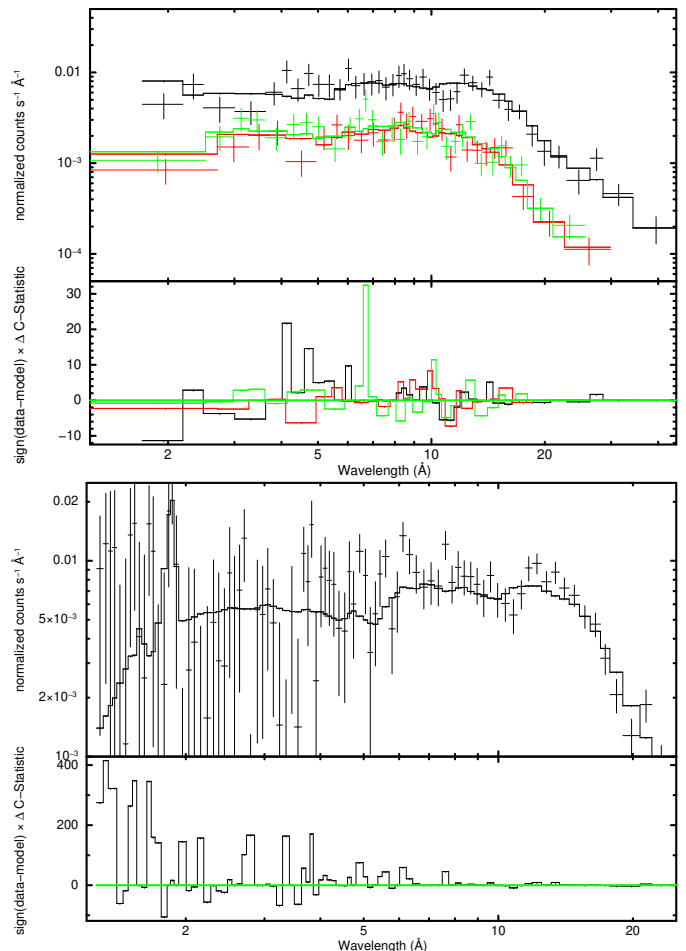


Fig. 1. Top panel: XMM-Newton pn (upper black crosses), and MOS1 and MOS2 (lower green and red crosses) spectra of HD 45166 where a suitable number of instrumental channels are binned, but not more than 300, to achieve at least a 3σ detection. Bottom panel: XMM-Newton unbinned EPIC pn spectra corrected for the instrument response (black crosses) of HD 45166, error bars corresponding to 1σ . The best-fit model is a combination of three thermal *vapec* models.

The XMM-Newton observations of HD 45166 were carried out on 2022-09-11 with a total duration ~ 20 ks (ObsID 0900520101). All three EPIC cameras were operated in the standard, full-frame mode. The “medium” UV filter was used for MOS cameras, while the “thin” filter was used for the pn. The observations were affected by episodes of high background. After rejecting these time intervals, the cumulative useful exposure time was ≈ 6 ks for the EPIC pn and ≈ 12 ks for the EPIC MOS cameras. No significant source variability is seen during these exposure times. The data were analyzed using the XMM-

¹ <https://obs.vla.nrao.edu/ect/>

Newton data analysis package SAS². The customary and the pipeline-reduced data are consistent.

Contrary to the radio, HD 45166 is clearly detected in all XMM-Newton cameras. The total EPIC count rate from the isolated X-ray source at the position of HD 45166 is $0.23 \pm 0.01 \text{ s}^{-1}$. The X-ray spectra and light curves of HD 45166 were extracted using standard procedures from a region with a radius $\approx 20''$. The background area was chosen to be nearby the star and free of X-ray sources. There are ≈ 1100 spectral data counts registered by the pn camera, while MOS cameras registered ≈ 1040 spectral counts.

To analyze the X-ray spectra of HD 45166 we used the standard spectral fitting software xSPEC (Arnaud 1996). The abundances were set to the HD 45166 abundances (Shenar et al. 2023) using the method outlined in Oskinova et al. (2012, 2020). In all spectral models, the absorption in the interstellar medium is included using the *tbabs* model (Wilms et al. 2000). Distance and reddening of HD 45166 are reported in Table 1.

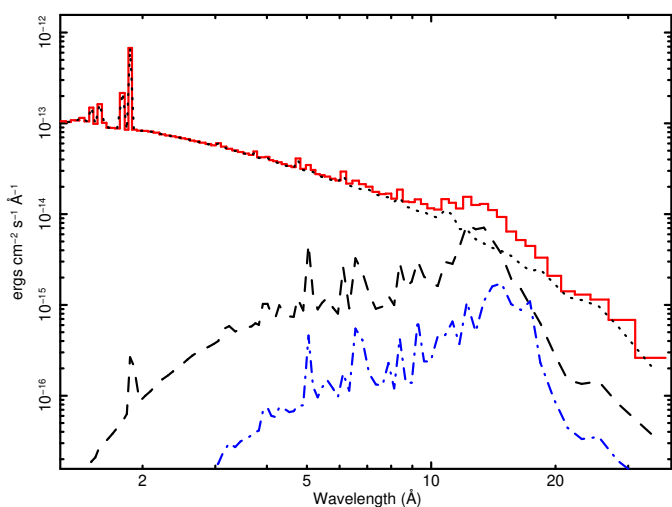


Fig. 2. Contributions from individual model components to the best-fit spectral models. *Left panel:* three temperature thermal model. The three lines (blue dashed-dotted, black dashed, black dotted) show spectral models corresponding to individual components (see Table 3). The red solid line shows the best fit combined model.

3. Results

3.1. X-ray diagnostic of the hot plasma

The HD 45166 system contains a non-magnetic B7 V-type star. Late B-type non-magnetic stars do not emit X-rays (Stelzer et al. 2005; Evans et al. 2011), therefore we attribute all X-rays detected in HD 45166 only to its helium star companion.

X-ray spectra of HD 45166 are shown in top panel of Fig. 1. The corresponding unbinned EPIC pn spectrum of HD 45166 is shown in bottom panel of Fig. 1, where a prominent emission line at $\lambda \approx 1.87 \text{ \AA}$ is clearly seen. This line belongs to the He-like Fe xxv ion which has a peak emissivity at $kT = 5.4 \text{ keV}$ ($T \approx 60 \text{ MK}$).

To determine the physical conditions of the plasma, we fitted the observed spectra using the Astrophysical Plasma Emission Code “*apec*” (Smith et al. 2001), that is a state-of-the-art code able to model a thermal optically thin plasma in collisional equilibrium. We used the *vaptec* version of the code which allows for

Table 3. X-ray spectral parameters derived from the XMM-Newton EPIC observations of HD 45166 assuming a three-temperature thermal plasma (*vaptec*) model and a thermal (*vaptec*) plus a power-law model, both models corrected for the interstellar absorption using the *tbabs* model. The errors are at 68% confidence level. The abundances are set to those deduced from the spectral analysis of optical and UV spectra of HD 45166 Shenar et al. (2023). The corresponding spectral fits are shown in Fig. 1. The contributions of each spectral component are shown in Fig. 2.

Three temperature thermal model	
N_{H} [10^{21} cm^{-2}]	1.2 ± 0.3
kT_1 [keV]	0.5 ± 0.3
EM_1 [10^{53} cm^{-3}]	1.1 ± 0.6
kT_2 [keV]	0.96 ± 0.21
EM_2 [10^{53} cm^{-3}]	1.3 ± 0.6
kT_3 [keV]	5.76 ± 0.95
EM_3 [10^{53} cm^{-3}]	20.2 ± 1.21
Flux [$10^{-13} \text{ erg cm}^{-2} \text{ s}^{-1}$]	4.1 ± 0.2
L_{X}^{a} [erg s^{-1}]	$(6.1 \pm 0.2) \times 10^{31}$
$\log(L_{\text{X}}/L_{\text{bol}})$	-5.63 ± 0.05
Fit statistic: χ^2 with 96 d.o.f.	116

^a intrinsic (dereddened) X-ray luminosity in the 0.2–12 keV energy band at the distance of 991 pc

non-solar abundances. The simulated spectrum superimposed to the observed one (binned and unbinned) is pictured in Fig. 1. The corresponding model parameters are shown in Table 3. Applying the relation $N_{\text{H,ISM}} = E_{B-V} \cdot 6.12 \times 10^{21} \text{ cm}^{-2}$ (Gudennavar et al. 2012), the interstellar column density is $(1.28 \pm 0.06) \times 10^{21} \text{ cm}^{-2}$. This is consistent with the N_{H} values inferred from the adopted X-ray model (see Table 3). Adopting the distance and the reddening from Table 1, the X-ray luminosity of HD 45166 (Table 3) is $\log(L_{\text{X}} [\text{erg s}^{-1}]) \approx 31.8$ corresponding to a ratio between X-ray and bolometric luminosity of $\log(L_{\text{X}}/L_{\text{bol}}) \approx -5.6$, i.e. among the highest ratios of known OB and WR-type stars without a compact binary companion (Nazé et al. 2014; Nebot Gómez-Morán & Oskinova 2018).

The combination of three temperature components is sufficient to fit the low-resolution X-ray spectrum of HD 45166. The individual model components are shown in Fig. 2. The lower temperature plasma components have $T \approx 6$ and 13 MK , whereas the highest temperature plasma has $T \approx 70 \text{ MK}$ ($kT \approx 5.7 \text{ keV}$), the largest emission measure (EM) among the three plasma components (Table 3), and is also responsible of the short wavelengths ($\lambda < 2 \text{ \AA}$) emission lines. To explain this high temperature by strong shocks invoking the Rankine-Hugoniot condition, where the temperature of the plasma after the shock is related to the pre-shock velocity as follows: $T \approx 14 \text{ MK} \times V_3^2$, where $V_3 = V/(10^3 \text{ km s}^{-1})$, a velocity jump of about 2200 km s^{-1} is required. Therefore, if X-rays originate from shocks occurring in the magnetically confined wind, the three thermal components could be the tracers of the temperature range of the regions where the shocks dissipate energy.

3.2. Radio diagnostic of the stellar wind

Any ionized stellar wind also emits thermal radio. For a spherical non-magnetic wind, the radio spectrum is described by $S_{\nu} \propto \dot{M}^{4/3} v^{0.6}$ (Wright & Barlow 1975; Panagia & Felli 1975), with the radio flux then providing a measure of the mass-loss rate. The full expression for calculating the theoretical spectrum of

² www.cosmos.esa.int/web/xmm-newton/what-is-sas

thermal radio emission from a stellar wind is given by Scuderi et al. (1998):

$$S_\nu = 7.26 \left(\frac{\nu}{10 \text{ GHz}} \right)^{0.6} \left(\frac{T_e}{10^4 \text{ K}} \right)^{0.1} \left(\frac{\dot{M}}{10^{-6} M_\odot \text{ yr}^{-1}} \right)^{4/3} \left(\frac{1.3 V_\infty}{100 \text{ km s}^{-1}} \right)^{-4/3} \left(\frac{d}{10^3 \text{ pc}} \right)^{-2} \text{ mJy}, \quad (1)$$

where the wind temperature (T_e) is assumed to be 85% of the effective stellar temperature.

No radio emission is detected at the position of HD 45166 and only upper limits on flux in three radio bands could be determined. Once fixed the terminal wind velocity in the Eq. (1), we can use the stringent upper limits on the fluxes in three radio bands (lying in the range 15–24 μJy , that is the 3σ detection threshold estimated by the map noises listed in Table 2) to constrain the mass-loss rate of the stellar wind.

In the absence of a strong globally organized magnetic field, the mass-loss rate, $\dot{M}(B=0)$, could be theoretically predicted and empirically measured by conventional spectroscopic methods. The strong, likely dipolar, magnetic field of the qWR star should strongly alter the topology of its stellar wind. While at low magnetic latitudes the wind is trapped, it is free to escape from the magnetic polar regions. It is reasonable to expect that the radial component of the polar wind is larger compared to the wind at low magnetic latitudes, which is trapped by the magnetic field and forced to flow along the magnetic field lines, thus the wind speed has no radial component near the magnetic equator. This may explain the differences between the wind terminal velocities at the equator and the pole ($V_\infty^{\text{eq}} \approx 425 \text{ km s}^{-1}$ and $V_\infty^{\text{pole}} \approx 1200 \text{ km s}^{-1}$; Groh et al. 2008).

The wind of the qWR star is expected to be confined by the dipole magnetic field up to the Alfvén radius, and only beyond it the ionized material can escape like a nearly spherical non-magnetic wind. At a large distance, the stellar wind which emerges from the polar regions fills a major fraction of the spherical volume. Therefore, the upper limit on radio emission allows to establish an upper limit on the mass-loss rate of the escaping wind. The strongest constraint for the mass loss rate of the freely escaping wind is given by the observation in the 15 GHz band which has the highest sensitivity (see Table 2) corresponding to a 3σ detection threshold of 15 μJy . We calculated radio spectra using the Eq. (1) varying only the parameter \dot{M} , while the terminal velocity was fixed to $V_\infty^{\text{pole}} = 1200 \text{ km s}^{-1}$.

The maximum mass-loss rate of the qWR star producing thermal radio emission with an emission level that does not contradict the VLA non-detection is $\dot{M}_{\text{max}} = 1.1 \times 10^{-7} M_\odot \text{ yr}^{-1}$, which is about a factor of two lower than the mass-loss rate of $2.2 \times 10^{-7} M_\odot \text{ yr}^{-1}$ found by Groh et al. (2008). The corresponding theoretical wind spectrum is pictured in Fig. 3 (black solid line). Assuming as a check the slower equatorial wind velocity, $V_\infty^{\text{eq}} = 425 \text{ km s}^{-1}$, a mass-loss rate of about $3.9 \times 10^{-8} M_\odot \text{ yr}^{-1}$, that is lower than \dot{M}_{max} , is required to be consistent with the upper limits in radio. Therefore, our radio observations definitively rule out the wind parameter combination corresponding to the lower value of the terminal wind velocity, $V_\infty = 425 \text{ km s}^{-1}$, and the mass-loss rate of $2.2 \times 10^{-7} M_\odot \text{ yr}^{-1}$ (Groh et al. 2008) as global properties of the wind escaping from the qWR star.

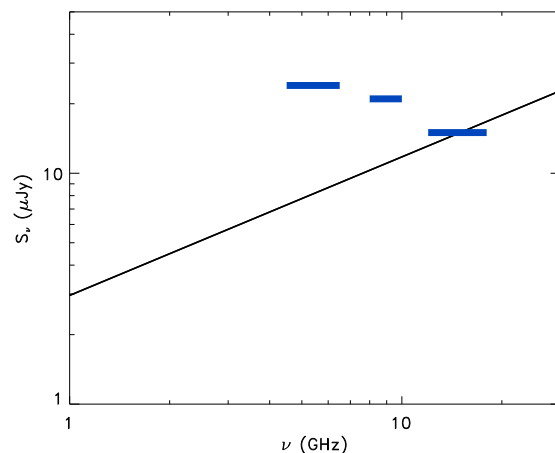


Fig. 3. The blue boxes correspond to the 3σ noise levels measured at the sky position of HD 45166 in radio maps obtained at the three observed bands, providing the detection threshold. The lengths of blue boxes show the bandpass for the receivers (see Table 2). The black solid line displays the theoretical thermal wind’s spectrum corresponding to the maximum emission level that is compatible with the non-detection below the 3σ threshold ($\dot{M}_{\text{max}} = 1.1 \times 10^{-7} M_\odot \text{ yr}^{-1}$).

4. X-rays from the wind of the highly magnetized helium star in the HD 45166 system

4.1. Thermal X-ray emission from the magnetic qWR

To quantify the X-rays emitted by the plasma heated in the framework of the MCWS model, time-dependent MHD simulations included a full energy equation with radiative cooling were performed by ud-Doula et al. (2014); their analysis of how the associated X-ray emission is controlled by a cooling-regulated ‘shock retreat’ led to a semi-analytic ‘XADM’ formalism. Once assigned the luminosity, mass, and radius of the star, the XADM model allows to predict the level and hardness of the intrinsic emitted X-rays as a function of the polar strength of the dipole field B_p , the mass-loss rate $\dot{M}(B=0)$, and the terminal speed V_∞ of the stellar wind expected in the absence of magnetic field. The agreement with observations is reached by scaling the predicted X-ray luminosity by an order of magnitude (Nazé et al. 2014). The 10% empirical reduction of the XADM prediction is to account for the lower X-ray emission expected from the dynamic infall of the trapped material, which is not considered in the idealized XADM model. In the following, we scale down the XADM predictions by an order of magnitude.

We modify the XADM formalism to account for highly unusual properties of the qWR star in HD 45166. For simplicity, we assume a pure helium wind. Furthermore, the polar field strengths is assumed equal to the average field ($\langle B \rangle = 43 \text{ kG}$). Usually, the polar strength is expected higher than the average, but the particular geometry of the qWR (i.e. the dipole is seen pole-on) makes this approximation reasonable.

Using stellar radius and bolometric luminosity reported in Table 1, the left panel of Fig. 4 shows the contour of the predicted $\log(L_X/L_{\text{bol}})$ (above 0.3 keV) set to the luminosity derived from the X-ray observations ($\log(L_{X,\text{obs}}/L_{\text{bol}}) = -5.6$; Table 3) as a function of non-magnetized wind mass-loss rate and terminal speed. The horizontal blue and red dashed lines mark respectively the limits of the range of the terminal speed values explored. For convenience the lower limit (V_∞^{slow}) has been fixed at 1200 km s^{-1} , that is the empirical wind speed value (Willis

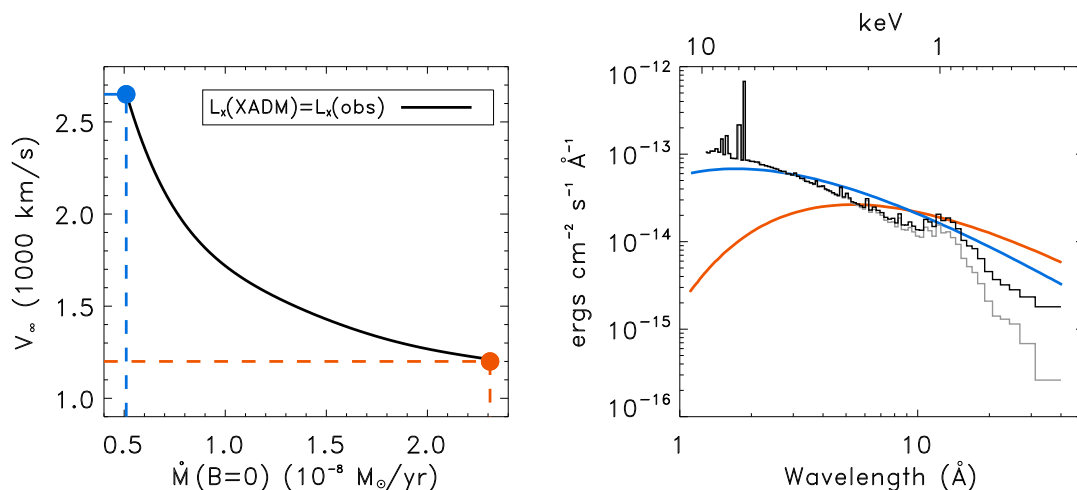


Fig. 4. Left: Diagram of the wind parameters of a non-magnetized star; terminal velocity vs mass-loss rate (the two wind parameters are the free parameters of the XADM model). The black curve represents the loci of the $\dot{M}(B=0)$ and V_∞ combination where the XADM model predicts X-ray luminosity coinciding with the empirically determined for the qWR star (Table 3). The red and blue horizontal dashed lines mark respectively the lower and upper limits of the range of terminal wind speed values analyzed, with $\dot{M}(B=0)$ tuned to match the observed X-ray luminosity along the black contour ($\log(L_X/L_{\text{bol}}) = -5.6$). Right: Associated model X-ray spectra for the fast (blue solid line) and the slower wind model (red solid line). For comparison, the X-ray spectrum of HD 45166 provided by the 3T model without the ISM absorption effect is also displayed (black solid line), the grey solid line is the X-ray spectrum with absorption shown in the left panel of Fig. 2.

et al. 1989), and the upper limit (V_∞^{fast}) at 2650 km s^{-1} , which is the value predicted by Vink (2017) for a $2 M_\odot$ helium star without magnetic field. The corresponding vertical dashed lines mark the associated mass-loss rates, $\dot{M}(B=0) = 0.51 \times 10^{-8} M_\odot \text{ yr}^{-1}$ and $2.3 \times 10^{-8} M_\odot \text{ yr}^{-1}$.

The right panel of Fig. 4 compares the model X-ray spectra corresponding to the velocities extrema, slow (red) and fast (blue). The XADM model with the fast wind has a hard X-ray component not predicted by the model with slower wind, with also a steeper overall decline at longer wavelengths. The qualitative comparison between the XADM synthetic spectra with the best-fit X-ray spectrum, provided by the pure thermal model once the ISM absorption effect is removed, evidences that the X-ray spectral behavior of HD 45166 is closer to the XADM fast wind model, giving also the feeling that the terminal wind speed could be higher than the fixed upper limit.

Thus the XADM modeling provides an estimate of the combination of wind parameters (mass-loss rate and terminal wind speed) by comparing the shapes of the simulated and observed X-ray spectra. Our analysis showed that a wind with parameters close to those theoretically predicted for a non-magnetic naked helium star with 2 solar masses ($\dot{M}_{\text{th}} \approx 0.4 \times 10^{-8} M_\odot \text{ yr}^{-1}$ and $V_\infty^{\text{th}} = 2650 \text{ km s}^{-1}$; Vink 2017) is consistent with the X-ray observations.

4.2. Constraints on the wind's parameters of the magnetic qWR

In plasma theory, the ratio between the gas pressure and the magnetic pressure of a stationary plasma defines the parameter β . In the case of a supersonic stellar wind channeled by a dipolar magnetic field, the thermal pressure is replaced by the ram pressure of the wind (Altschuler & Newkirk 1969). Then, the reciprocal of plasma- β is:

$$\eta_* = \frac{B^2/8\pi}{\rho_w V_\infty^2/2} \approx \frac{B_p^2 R_*^2}{4\dot{M}(B=0)V_\infty}, \quad (2)$$

that is the magnetic confinement parameter which characterizes the capability of the stellar magnetic field to channel the wind, which starts on the stellar surface as a radial wind, that is, as a simple non-magnetic spherical wind (ud-Doula & Owocki 2002). In this description, the Alfvén radius is given by the following relation (ud-Doula et al. 2008):

$$R_A \approx 0.3 + \eta_*^{1/4}. \quad (3)$$

Assuming a simple dipole magnetic field, the wind emerging from the stellar surface ($\dot{M}(B=0)$) could actually leave the magnetosphere only from the magnetic polar caps. The polar caps are delimited by the northern and southern polar rings located by the magnetic latitude of the footprints of the last closed magnetic field line, that is the line crossing the magnetic equatorial plane at the distance equal to $R_c \approx 1 + 0.7(R_A - 1)$ stellar radii. Following ud-Doula et al. (2008), the wind material lost from a magnetic star can be estimated using the scaling relation:

$$\dot{M} \approx \dot{M}(B=0) \times (1 - \sqrt{1 - 1/R_c}). \quad (4)$$

With a polar magnetic field strength equal to 43 kG, the associated magnetic confinement parameter, calculated using the Eq. (2) ($V_\infty = 2650 \text{ km s}^{-1}$ and $\dot{M}(B=0) = 0.51 \times 10^{-8} M_\odot \text{ yr}^{-1}$), is $\eta_* = 20500$. The corresponding Alfvén radius calculated using Eq. (3) is $R_A/R_* = 12.3$.

In summary, the wind of the qWR star is expected to be confined by the closed dipole magnetic field lines up to the Alfvén radius, and only beyond this radius the ionized material can escape like a nearly spherical non-magnetic wind. The fraction of the wind mass that escapes can be estimated using the Eq. (4), that is about 6% of the wind emerging from the whole stellar surface. The corresponding actual mass-loss rate is $\approx 3 \times 10^{-10} M_\odot \text{ yr}^{-1}$, that is about three orders of magnitudes lower than the upper limit constrained by the radio observations (Sect. 3.2), with a related thermal radio emission level of $\approx 5 \times 10^{-3} \mu\text{Jy}$ (calculated using Eq. (1)).

The wind topology of the qWR is strongly affected by the strong magnetic field. Only a fraction of the fast wind ($V_\infty^{\text{fast}} =$

Table 4. Magnetospheric parameters of the qWR star.

Parameter	Symbol	Unit	Value
Mass-loss rate in absence of magnetic field derived from the XADM model	$\dot{M}(B=0)$	$M_{\odot} \text{ yr}^{-1}$	5.1×10^{-9}
Terminal wind velocity theoretically predicted in absence of magnetic field	$V_{\infty}^{\text{th}} \equiv V_{\infty}^{\text{fast}}$	km s^{-1}	2650
Wind confinement parameter	η_*	-	20500
Alfvén radius	R_A	R_*	12.3
Mass-loss rate actually lost from the magnetic qWR	\dot{M}	$M_{\odot} \text{ yr}^{-1}$	$\approx 3 \times 10^{-10}$
Radial wind velocity measured from spectroscopy	$V_{\infty}(\text{obs.})^{\dagger\dagger} \equiv V_{\infty}^{\text{slow}}$	km s^{-1}	1200
Kepler radius	R_K	R_*	≈ 150

[†] Vink (2017). ^{††} Willis et al. (1989);

2650 km s^{-1}) can escape from the magnetosphere at high magnetic latitudes, becoming nearly spherical far from the star. Due to the larger area covered by the freely expanding spherical wind, according to the principle of mass continuity, the non-magnetic spherical wind is expected to expand outside the Alfvén surface at a slower velocity with respect to the fast wind velocity required to reproduce the X-ray spectrum of the qWR star. Therefore, the velocity measured in the UV spectrum ($V_{\infty}(\text{obs.}) = 1200 \text{ km s}^{-1}$) is considered as an empirical estimate of the terminal wind velocity of the large-scale spherical wind material actually lost from the qWR star. Figure 5 shows a cartoon that visualizes the scenario described above.

5. On the lack of detection of non-thermal radio emission from the qWR in HD 45166

The qWR star is strongly magnetized, and the combined presence of ionized material (wind plasma trapped by the closed magnetic field lines) and strong magnetic field could provide suitable conditions for non-thermal radio emission powered by the gyro-synchrotron mechanism. In the following we use the detection threshold obtained by the VLA observations to constrain the plasma parameters regulating a non-thermal radio emission that is compatible with the non-detection of radio emission from HD 45166.

5.1. On the non-thermal electron production within the magnetosphere of the qWR

To better understand the properties of the qWR star, we first consider the case of magnetic ApBp-stars. These are also hot stars with radiatively driven stellar winds confined by strong magnetic field. Hence, ApBp-stars provide a useful physical analogy to the “one of its kind” magnetic helium star in HD 45166. The magnetic ApBp-stars have magnetospheres filled by plasma radiating X-rays; furthermore, these magnetic stars are well-studied non-thermal radio sources. The well-ordered and stable magnetospheres of fast-rotating ApBp stars share a common physical mechanism for supporting the generation of non-thermal electrons, which explains their observational features ranging from the X-ray to radio regime. A general scaling relationship for non-thermal radio emission holds from stars at the top of the main sequence down to the ultra-cool dwarfs and to the planet Jupiter (Leto et al. 2021). This is empirically confirmed for ApBp stars (Shultz et al. 2022). The underlying physical process could be related to the breakout events that are predicted in the centrifugally supported magnetospheres (CM) of fast rotating stars (Owocki et al. 2022). In this case, the radio luminosity is directly related to the power released by the centrifugal breakout events (CBO). In particular, the relation between the spectral radio lu-

minosity and the power of the centrifugal breakouts (L_{CBO}) is: $L_{\nu, \text{rad}} = 10^{-19} L_{\text{CBO}} \text{ Hz}^{-1}$ (Leto et al. 2022), where

$$L_{\text{CBO}} = \frac{B_p^2 R_*^3}{P_{\text{rot}}} \times W \quad (\text{erg s}^{-1}), \quad (5)$$

and $W = 2\pi R_*/(P_{\text{rot}} \sqrt{GM_*/R_*})$ is the dimensionless critical rotation parameter, defined by the ratio between equatorial velocity and orbital velocity, with G being the gravitational constant.

Using the stellar parameters reported in Table 1 it follows that $W \approx 5.4 \times 10^{-4}$ for the qWR star. Eq. (5) predicts the spectral radio luminosity $L_{\nu, \text{rad}} \approx 2.1 \times 10^{12} \text{ erg s}^{-1} \text{ Hz}^{-1}$, corresponding to the flux of $\approx 1.8 \times 10^{-3} \mu\text{Jy}$, which, in the frequency range covered by the VLA observations, is lower than the expected flux level of the thermal radio emission constrained in Sect. 4. Hence, the CBOs are inefficient as a mechanism for the acceleration of electrons in the magnetic qWR star. This is not surprising since the key condition for the generation of CMs is the Kepler corotation radius (R_K) which is smaller than the Alfvén radius. The Kepler radius is given by $R_K = W^{-2/3} R_*$ (Petit et al. 2013). We estimate $R_K \approx 150 R_*$, which is about an order of magnitude larger than the Alfvén radius estimated in Sect. 4.2 (Table 4), this implies that the qWR does not support a centrifugal magnetosphere.

Let’s consider whether stellar wind might play a role in particle acceleration. Indeed, the wind strength in the qWR star is much higher compared to the ApBp-type stars (Oskinova et al. 2011; Krtićka et al. 2019), and can break the magnetic field lines relatively close to the star ($R_A \approx 12 R_*$) where the local magnetic field is high enough to trigger plasma effects responsible for non-thermal radio emission (Andre et al. 1988). At distances larger than R_A , the magnetic fields no longer controls the wind. The equatorial regions just outside the Alfvén surface are transition regions from the magnetic-dominated to the wind-dominated zones, where the closed dipole-like magnetic field configuration becomes open. These are likely sites of large-scale magnetic field reorganization, with the consequent formation of a magneto-disk, possibly originating current sheets. In these regions, magnetic field lines of opposite polarity exist and magnetic reconnections may occur, where electrons can be accelerated up to relativistic energies (Usov & Melrose 1992). This acceleration mechanism has been also taken into account to predict the emission of gamma rays from a magnetic hot massive star with a strong wind and DM magnetosphere (Bednarek 2021).

5.2. Modeling the non-thermal radio emission from the qWR

Both ingredients for the production of non-thermal radio emission – magnetic field and relativistic electrons – could be expected in the magnetosphere of the qWR star. The predicted level

and the spectral shape of emerging non-thermal radio radiation depend on two key factors: (1) the acceleration efficiency which dictates how much non-thermal radio radiation is produced, and (2) the wind optical depth which determines how much non-thermal radiation is able to escape.

To calculate the spectrum of non-thermal radio emission we employ 3D model of a dipole shaped magnetosphere (Trigilio et al. 2004; Leto et al. 2006). After sampling the space surrounding the star by using a cartesian grid with three different sampling steps, once assigned the radio frequency (ν), all the physical parameters needed for the calculation of the gyro-synchrotron absorption and emission coefficients are calculated in each grid point and the radiative transfer equation is numerically integrated along ray paths parallel to the line of sight. The orientation of the dipole-shaped magnetosphere with respect to the observer can be arbitrarily varied, this allows a proper reproduction of the measured rotational modulation of the non-thermal radio emission from co-rotating magnetospheres of ApBp-type stars with magnetic dipole axis not aligned to the rotation axis (Leto et al. 2012, 2017, 2018, 2020b,a). Even if the most likely magnetic field geometry of the qWR star suggest a pole-on view (Shenar et al. 2023), for completeness, we also performed model simulations for the equator-on view (corresponding to the magnetic axis perpendicular to the line of sight).

To compute the gyro-synchrotron radio spectrum of the qWR, we conservatively assumed a polar field strength $B_p = 43$ kG, as already discussed in Sect. 4.1. The relativistic electrons are assumed power-law energy distributed, $N_{\text{rel}}(E) \propto E^{-\delta}$, where $N_{\text{rel}}(E)$ is the number density of the electrons of energy E . Similar to the case of the ApBp-magnetic stars (Leto et al. 2021), a low energy cutoff at $E = 10$ keV for the non-thermal electrons is adopted, and the spectral index of the energy distribution of the non-thermal electrons is assumed as $\delta = 2.5$. The region where these non-thermal electrons move is defined by the Alfvén radius. We assume that the thermal plasma density located below R_A is a function of both the radial distance and the magnetic colatitude. For crude estimates, we make use of the density law valid for a magnetically trapped wind retrieved by modeling a slow-rotating dynamical magnetosphere with an analytical approach (ADM model) (Owocki et al. 2016). The adopted parameters of the trapped wind are $\dot{M}(B=0)$ and V_∞^{th} , both listed in Table 4.

The only free parameter is the column density of the relativistic electrons injected at the distance of R_A , which is the number density of the relativistic electron times the equatorial linear size of the magnetic shell where they freely move. This size is related to the size of the magneto-disk where the non-thermal electrons are likely accelerated. Finally, to calculate the emerging non-thermal radio spectrum of the qWR, we also account for the attenuation of radio waves traveling through the outer layers filled by thermal plasma coming from the stellar wind, which can be parameterized by the radius of the wind region that is optically thick at a given radio frequency (see Figure 5).

According to Panagia & Felli (1975), the radius of the optically thick radio photosphere of a spherical ionized wind is:

$$R_\nu \approx 6.23 \times 10^{14} \left(\frac{\nu}{10 \text{ GHz}} \right)^{-0.7} \left(\frac{T_e}{10^4 \text{ K}} \right)^{-0.45} \left(\frac{\dot{M}}{10^{-5} M_\odot \text{ yr}^{-1}} \right)^{2/3} \left(\frac{V_\infty}{10^3 \text{ km s}^{-1}} \right)^{-2/3} \text{ cm.} \quad (6)$$

Using the mass-loss rate of the wind material actually lost from the magnetic qWR star ($\dot{M} = 3 \times 10^{-10} M_\odot \text{ yr}^{-1}$) and assum-

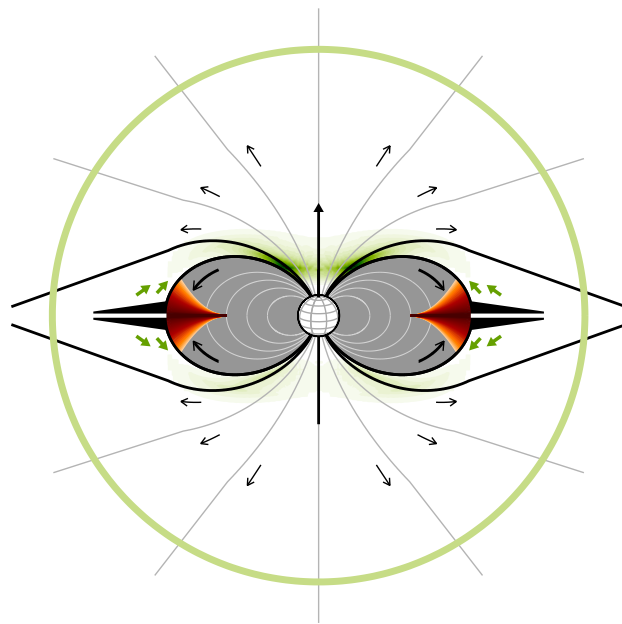


Fig. 5. Meridional cross-section of the dipole-dominated magnetosphere of HD 45166 (not to scale). At distances smaller than the Alfvén radius (R_A) the magnetic field lines are closed. The last closed field lines (marked by the black thick solid line) locates the R_A . At larger distances, the ionized wind opens the magnetic field lines. The region where the magnetic field traps the stellar wind is shaded. Outside of the Alfvén surface, the stellar wind freely escapes (black arrows). At lower latitudes, the fast wind plasma streams arising from opposite hemispheres (thick black arrows) collide and shock. According to the XADM model, the shock heats the plasma producing X-rays (red regions). The equatorial magneto-disk farther than R_A (thick black areas) is likely the site of acceleration of electrons (green solid arrows) via magnetic reconnections. Such non-thermal electron population moving within a magnetic shell (delimited by the black and thick solid lines) radiates at the radio regime by the gyro-synchrotron emission mechanism. The outer boundary where the non-thermal electrons diffuse is pictured by the solid black open field line. The relativistic electrons radiate in radio bands by a non-thermal emission mechanism (green-shaded regions). The large green circle outlines the optically thick radio photosphere of the freely escaping ionized wind.

ing spherically expanding wind outside the Alfvén radius ($R_A \approx 12 R_\odot$); see Sect. 4.2) with velocity $V_\infty(\text{obs.}) = 1200 \text{ km s}^{-1}$, the radius of the radio photosphere at $\nu = 100 \text{ MHz}$ is $R_{0.1 \text{ GHz}} \approx 110 R_*$, that at $\nu = 10 \text{ GHz}$ decreases to $R_{10 \text{ GHz}} \approx 4 R_*$ that is lower than R_A .

To search for suitable conditions for the VLA non-detection, we computed models progressively decreasing the column density of the non-thermal electrons. We performed model simulation covering a wide frequency range extending to the low frequencies domain. Outside the magnetospheric volume, the wind material freely escaping has been roughly assumed spherical, and the continuity equation $\rho = \dot{M}/4\pi r^2 v(r)$ of the wind expanding according to a velocity law $v(r) = V_\infty(1 - R_*/r)$ was adopted. To include absorption, we integrate the radiative transfer equation within a huge cubic volume with lateral size much larger than the radio photosphere corresponding to the lowest analyzed frequency (100 MHz), i.e. $600 R_*$. The small cubic element with a side of $0.25 R_*$ is used to sample the inner cube with side $15 R_*$. The intermediate sampling of $0.5 R_*$ was adopted for the regions within the cube with side $40 R_*$. At larger distances a sampling step of $4 R_*$ is adopted.

The simulated gyro-synchrotron spectra computed for the two extrema magnetospheric orientations (pole-on view and equator-on view) and compatible with the VLA upper limits are pictured in Fig. 6 (grey region). The corresponding limit on the non-thermal electrons column density is $\approx 3 \times 10^{15} \text{ cm}^{-2}$. For comparison, in fast rotating early-type magnetic stars, the column density of non-thermal electrons able to reproduce their observed gyro-synchrotron radio spectra is on average 10^{16} cm^{-2} (Leto et al. 2021). This evidences that, even assuming a radio emission level just below the VLA detection threshold, the possible acceleration mechanisms of non-thermal electrons operating within the DM of the qWR star in HD 45166 is likely less efficient than the CBOs inside the centrifugal magnetospheres surrounding the ApBp-type stars.

The wind's radio photosphere depends on frequency, as $\propto \nu^{-0.7}$ (Eq. (6)), therefore, the wind absorption effect increases at lower frequencies. In fact, looking at Fig. 6, the possible non-thermal gyro-synchrotron emission from the qWR star is fully absorbed at the lower frequency range. Despite the rough sampling step adopted at a large distance, this discrete integration of the radiative transfer equation produces a fully absorbed non-thermal radio spectrum at the lower frequencies ($\nu \lesssim 300 \text{ MHz}$) almost indistinguishable from the theoretical radio spectrum of a spherical wind predicted by the Eq. (1) (adopted wind parameters: $\dot{M} = 3 \times 10^{-10} M_{\odot} \text{ yr}^{-1}$; $V_{\infty} = 1200 \text{ km s}^{-1}$) depicted in Fig. 6 by the black dashed line, with the wind absorption effect that is non negligible for the gyro-synchrotron emission up to frequencies close to $\approx 1 \text{ GHz}$. On the other hand, the wind actually lost from the qWR is too weak to provide significant absorbing effects in the VLA observing bands.

5.3. Other possible cases for the model application

The modeling approach presented in this paper represents the computational implementation of the qualitative model of a non-thermal stellar radio source embedded within a large-scale spherical environment of ionized material released by the freely escaping wind (Andre et al. 1988) which should be applied also in cases of other hot magnetic stars that originate powerful stellar winds. I.e. the highly magnetized O7-type star NGC 1624-2, which is intrinsically very bright at the X-rays, but its X-ray emission is strongly attenuated by the wind material trapped within the stellar magnetosphere (Petit et al. 2015) and, similarly to HD 45166, NGC 1624-2 was undetected at the radio regime (Kurapati et al. 2017). Or to the case of the magnetic O7.5-type star member of the O+O binary system HD 47129, which has similar X-ray luminosity of HD 45166 (Nazé et al. 2014) and further shows an interesting radio spectral behavior. This star was undetected at the lower frequency but has an almost flat emission at the other two highest frequencies (Kurapati et al. 2017). The spectral range covered by the HD 47129 radio measurements covers the spectral range of the radio measurements here reported. We highlight that the observed spectral behavior of HD 47129 is qualitatively in accordance with the synthetic radio spectra reported in this paper (see Fig. 6), but shifted in frequency, supporting the idea that non-thermal gyro-synchrotron radio emission may undergo frequency-dependent absorption effects provided by the large-scale surrounding ionized medium.

6. Summary and Conclusions

In this paper we report XMM-Newton and VLA measurements of the HD 45166 system composed by a non magnetic late B-type star and a highly magnetized quasi-WR star. The system

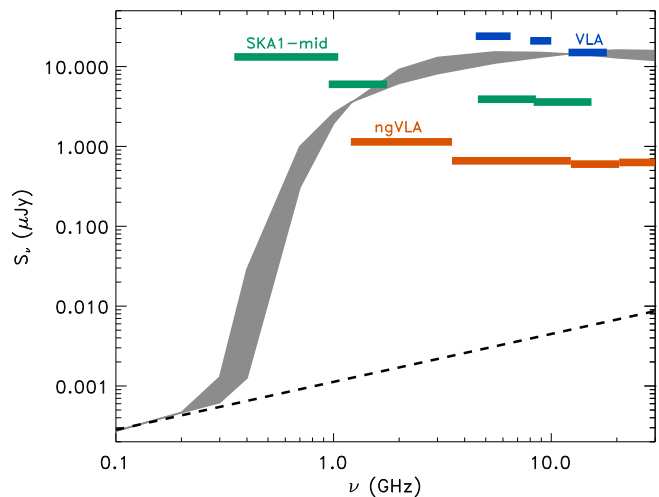


Fig. 6. Theoretical radio spectra of the qWR component in the HD 45166 system in comparison with the upper limits derived from the VLA observations (blue boxes). The black dashed line is for a spherical wind with mass-loss rate $\dot{M} = 3 \times 10^{-10} M_{\odot} \text{ yr}^{-1}$ and $V_{\infty} = 1200 \text{ km s}^{-1}$. The grey shaded area shows the variety of non-thermal gyro-synchrotron spectra computed for different orientations of the magnetosphere with respect to the observer, assuming two distinct values of the spectral index δ , and accounting for the attenuation in the stellar wind. The green boxes represent the expected 3σ threshold of the noise levels that will be reached with observations 1 hour long at the observing bands that will be provided by the forthcoming SKA1-mid. The orange boxes instead represent the expected 3σ threshold of the noise levels that will be achieved assuming the same integration time (1 hour) using the observing bands that will be provided by the future ngVLA.

has been clearly detected at the X-rays, but no radio counterpart has been found by the highly sensitive radio measurements.

The upper limit on radio emission allowed us to put robust observational constraints on the actual wind mass-loss rate of the the qWR star. Additionally, the detection of the emission line at $\lambda = 1.87 \text{ \AA}$ ($\sim 6.6 \text{ keV}$) in the X-ray spectrum is the observational evidence that very fast plasma streams exist within the magnetosphere of the qWR. The XADM model is able to explain the observed X-ray luminosity and spectrum shape (see Fig. 4). On the other hand, the magnetic field traps a large fraction of the wind reducing the amount of material effectively lost. We constrain the effective wind mass-loss rate of the magnetic qWR $\dot{M} \approx 3 \times 10^{-10} M_{\odot} \text{ yr}^{-1}$.

The qWR star component of the HD 45166 system has a mass of $2.03 \pm 0.44 M_{\odot}$, which is at least 0.15 solar masses above the Chandrasekhar limit of $1.44 M_{\odot}$. The time required to remove enough material via stellar wind to fall below the Chandrasekhar limit is 500 Myr, i.e. longer than the helium burning phase of a massive star with a He core of similar mass to the qWR which last a few Myr (Ritter et al. 2018).

We also explored the physical mechanisms able to produce radio emission from the magnetic qWR star, then providing constraints on the parameters that make it compatible with the upper limits measured by the VLA. We calculated the non-thermal radio spectrum taking into account the extinction effects. To explain that there is no non-thermal radio emission above the VLA detection threshold, we found that the non-thermal electron production has to be less efficient compared to the fast-rotating ApBp-type magnetic stars. Generally, in ApBp-type magnetic stars the gyro-synchrotron radio emission level correlates with

the stellar rotation speed (Leto et al. 2021) and therefore to the centrifugal breakouts power, which is the proposed driving mechanism for non-thermal electron production (Owocki et al. 2022). This is not the case of the magnetic qWR star in HD 45166 because it is a slow rotator with a DM, therefore not able to efficiently sustain rotationally supported acceleration mechanisms. Hence the non-thermal electron production is fundamentally different and less efficient compared to ApBp-type stars with CMs.

Studying of the radio spectrum of HD 45166 is an ideal science case for the SKA1-mid radio interferometer. The expected noiselevel at the available radio bands of SKA1-mid, operating between 350 MHz and 15 GHz, ranges between ≈ 1 and $\approx 4 \mu\text{Jy}$ for observations 1 hour long (green boxes in Fig. 6) (Braun et al. 2019). But even more powerful will be the future next generation VLA (ngVLA). Assuming radio observations 1 hour long, the ngVLA will allow us to explore the radio spectrum of HD 45166 with a sub μJy sensitivity level (orange boxes of Fig. 6) at all the available frequency bands (which will cover the frequency range from 1.2 up to 116 GHz) (Selina et al. 2018). The ngVLA will be able to definitely test the presence of non-thermal radio emission in HD 45166 to unveil the physical processes occurring within the magnetosphere of the qWR, which is a DM prototype.

To conclude, we have empirically demonstrated that the acceleration processes (if any) occurring within the magnetosphere of the slowly rotating qWR magnetic star in the HD 45166 system are less efficient than that occurring within the CMs of the fast rotating ApBp-type stars. We also evidenced that the theoretical recipe to estimate the wind parameters from non-magnetic helium stars fits well the case of the magnetically constrained wind of the qWR. Further, taking into account the magnetic nature of this evolved star, we estimated that the actual rate of mass lost from the magnetic qWR star is not able to remove a significant amount of mass. Hence, this (currently) unique object is likely to maintain its super-Chandrasekhar mass until its death and undergo a core-collapse supernova explosion producing a magnetar.

Acknowledgements. We thank the referee for his/her constructive comments that helped us to improve the paper. SO and AuD acknowledge support by the National Aeronautics and Space Administration under Grant No. 80NSSC22K0628 issued through the Astrophysics Theory Program. RI gratefully acknowledges support by the National Science Foundation under grant number AST-2009412. GAW acknowledges Discover Grant support from the Natural Sciences and Engineering Research Council (NSERC) of Canada.

References

- Altschuler, M. D. & Newkirk, G. 1969, *Solar Physics*, 9, 131
 Andre, P., Montmerle, T., Feigelson, E. D., Stine, P. C., & Klein, K.-L. 1988, *ApJ*, 335, 940
 Anger, C. J. 1933, *Harvard College Observatory Bulletin*, 891, 8
 Arnaud, K. A. 1996, in *Astronomical Society of the Pacific Conference Series*, Vol. 101, *Astronomical Data Analysis Software and Systems V*, ed. G. H. Jacoby & J. Barnes, 17
 Babcock, H. W. 1960, *ApJ*, 132, 521
 Babel, J. & Montmerle, T. 1997, *A&A*, 323, 121
 Bailer-Jones, C. A. L., Rybizki, J., Fouesneau, M., Demleitner, M., & Andrae, R. 2021, *AJ*, 161, 147
 Bednarek, W. 2021, *MNRAS*, 507, 3292
 Braun, R., Bonaldi, A., Bourke, T., Keane, E., & Wagg, J. 2019, arXiv e-prints, arXiv:1912.12699
 Castor, J. I., Abbott, D. C., & Klein, R. I. 1975, *ApJ*, 195, 157
 Das, B., Chandra, P., Shultz, M. E., et al. 2022, *MNRAS*, 517, 5756
 Dionne, D. & Robert, C. 2006, *ApJ*, 641, 252
 Doughty, C. & Finlator, K. 2021, *MNRAS*, 505, 2207
 Drake, S. A., Abbott, D. C., Bastian, T. S., et al. 1987, *ApJ*, 322, 902
 Drake, S. A., Linsky, J. L., Schmitt, J. H. M. M., & Rosso, C. 1994, *ApJ*, 420, 387
 Drout, M. R., Göteborg, Y., Ludwig, B. A., et al. 2023, arXiv e-prints, arXiv:2307.00061
 Evans, N. R., DeGioia-Eastwood, K., Gagné, M., et al. 2011, *ApJS*, 194, 13
 Gilkis, A. & Shenar, T. 2023, *MNRAS*, 518, 3541
 Göteborg, Y., de Mink, S. E., Groh, J. H., et al. 2018, *A&A*, 615, A78
 Groh, J. H., Oliveira, A. S., & Steiner, J. E. 2008, *A&A*, 485, 245
 Gudennavar, S. B., Bubbly, S. G., Preethi, K., & Murthy, J. 2012, *ApJS*, 199, 8
 Hamann, W. R., Gräfener, G., Liermann, A., et al. 2019, *A&A*, 625, A57
 Hiltner, W. A. & Schild, R. E. 1966, *ApJ*, 143, 770
 Krtićka, J., Mikulášek, Z., Henry, G. W., et al. 2019, *A&A*, 625, A34
 Kurapati, S., Chandra, P., Wade, G., et al. 2017, *MNRAS*, 465, 2160
 Leone, F., Triglilio, C., & Umama, G. 1994, *A&A*, 283, 908
 Leto, P., Oskinova, L. M., Buemi, C. S., et al. 2022, *MNRAS*, 515, 5523
 Leto, P., Triglilio, C., Buemi, C. S., et al. 2020a, *MNRAS*, 499, L72
 Leto, P., Triglilio, C., Buemi, C. S., Leone, F., & Umama, G. 2012, *MNRAS*, 423, 1766
 Leto, P., Triglilio, C., Buemi, C. S., Umama, G., & Leone, F. 2006, *A&A*, 458, 831
 Leto, P., Triglilio, C., Krtićka, J., et al. 2021, *MNRAS*, 507, 1979
 Leto, P., Triglilio, C., Leone, F., et al. 2020b, *MNRAS*, 493, 4657
 Leto, P., Triglilio, C., Oskinova, L., et al. 2017, *MNRAS*, 467, 2820
 Leto, P., Triglilio, C., Oskinova, L. M., et al. 2018, *MNRAS*, 476, 562
 Linsky, J. L., Drake, S. A., & Bastian, T. S. 1992, *ApJ*, 393, 341
 Nazé, Y., Petit, V., Rinbrand, M., et al. 2014, *ApJS*, 215, 10
 Nebot Gómez-Morán, A. & Oskinova, L. M. 2018, *A&A*, 620, A89
 Neubauer, F. J. & Aller, L. H. 1948, *ApJ*, 107, 281
 Oskinova, L. M., Gayley, K. G., Hamann, W. R., et al. 2012, *ApJ*, 747, L25
 Oskinova, L. M., Gvaramadze, V. V., Gräfener, G., Langer, N., & Todt, H. 2020, *A&A*, 644, L8
 Oskinova, L. M., Todt, H., Ignace, R., et al. 2011, *MNRAS*, 416, 1456
 Owocki, S. P., Shultz, M. E., ud-Doula, A., et al. 2022, *MNRAS*, 513, 1449
 Owocki, S. P., ud-Doula, A., Sundqvist, J. O., et al. 2016, *MNRAS*, 462, 3830
 Panagia, N. & Felli, M. 1975, *A&A*, 39, 1
 Petit, V., Cohen, D. H., Wade, G. A., et al. 2015, *MNRAS*, 453, 3288
 Petit, V., Owocki, S. P., Wade, G. A., et al. 2013, *MNRAS*, 429, 398
 Podsiadlowski, P., Joss, P. C., & Hsu, J. J. L. 1992, *ApJ*, 391, 246
 Ramachandran, V., Klencki, J., Sander, A. A. C., et al. 2023, *A&A*, 674, L12
 Ritter, C., Herwig, F., Jones, S., et al. 2018, *MNRAS*, 480, 538
 Robrade, J., Oskinova, L. M., Schmitt, J. H. M. M., Leto, P., & Triglilio, C. 2018, *A&A*, 619, A33
 Sander, A. A. C., Hamann, W. R., Todt, H., et al. 2019, *A&A*, 621, A92
 Scuderi, S., Panagia, N., Stanghellini, C., Triglilio, C., & Umama, G. 1998, *A&A*, 332, 251
 Selina, R. J., Murphy, E. J., McKinnon, M., et al. 2018, in *Astronomical Society of the Pacific Conference Series*, Vol. 517, *Science with a Next Generation Very Large Array*, ed. E. Murphy, 15
 Shenar, T., Gilkis, A., Vink, J. S., Sana, H., & Sander, A. A. C. 2020, *A&A*, 634, A79
 Shenar, T., Wade, G. A., Marchant, P., et al. 2023, *Science*, 381, 761
 Shultz, M. E., Owocki, S. P., ud-Doula, A., et al. 2022, *MNRAS*, 513, 1429
 Smith, R. K., Brickhouse, N. S., Liedahl, D. A., & Raymond, J. C. 2001, *ApJ*, 556, L91
 Stelzer, B., Flaccomio, E., Montmerle, T., et al. 2005, *ApJS*, 160, 557
 Triglilio, C., Leto, P., Leone, F., Umama, G., & Buemi, C. 2000, *A&A*, 362, 281
 Triglilio, C., Leto, P., Umama, G., Leone, F., & Buemi, C. S. 2004, *A&A*, 418, 593
 ud-Doula, A. & Nazé, Y. 2016, *Advances in Space Research*, 58, 680
 ud-Doula, A., Owocki, S., Townsend, R., Petit, V., & Cohen, D. 2014, *MNRAS*, 441, 3600
 ud-Doula, A. & Owocki, S. P. 2002, *ApJ*, 576, 413
 ud-Doula, A., Owocki, S. P., & Townsend, R. H. D. 2008, *MNRAS*, 385, 97
 ud-Doula, A., Sundqvist, J. O., Owocki, S. P., Petit, V., & Townsend, R. H. D. 2013, *MNRAS*, 428, 2723
 Usov, V. V. & Melrose, D. B. 1992, *ApJ*, 395, 575
 van Blerkom, D. 1978, *ApJ*, 225, 175
 Vink, J. S. 2017, *A&A*, 607, L8
 Willis, A. J., Howarth, I. D., Stickland, D. J., & Heap, S. R. 1989, *ApJ*, 347, 413
 Willis, A. J. & Stickland, D. J. 1983, *MNRAS*, 203, 619
 Wilms, J., Allen, A., & McCray, R. 2000, *ApJ*, 542, 914
 Woosley, S. E., Langer, N., & Weaver, T. A. 1995, *ApJ*, 448, 315
 Wright, A. E. & Barlow, M. J. 1975, *MNRAS*, 170, 41
 Yungelson, L., Kuranov, A., Postnov, K., et al. 2024, *A&A*, 683, A37